arXiv:2401.14726v1 [cs.CV] 26 Jan 2024

3D Reconstruction and New View Synthesis of Indoor Environments based on a Dual Neural Radiance Field

Zhenyu Bao*[1,2], Guibiao Liao [1,2], Zhongyuan Zhao [1,2], Kanglin Liu†[2], Qing Li†[2], Guoping Qiu [3,4]
[1]Peking University [2]Pengcheng Laboratory
[3]University of Nottingham [4]Shenzhen University

Abstract

Simultaneously achieving 3D reconstruction and new view synthesis for indoor environments has widespread applications but is technically very challenging. State-of-the-art methods based on implicit neural functions can achieve excellent 3D reconstruction results, but their performances on new view synthesis can be unsatisfactory. The exciting development of neural radiance field (NeRF) has revolutionized new view synthesis, however, NeRF-based models can fail to reconstruct clean geometric surfaces. We have developed a dual neural radiance field (Du-NeRF) to simultaneously achieve high-quality geometry reconstruction and view rendering. Du-NeRF contains two geometric fields, one derived from the SDF field to facilitate geometric reconstruction and the other derived from the density field to boost new view synthesis. One of the innovative features of Du-NeRF is that it decouples a view-independent component from the density field and uses it as a label to supervise the learning process of the SDF field. This reduces shape-radiance ambiguity and enables geometry and color to benefit from each other during the learning process. Extensive experiments demonstrate that Du-NeRF can significantly improve the performance of novel view synthesis and 3D reconstruction for indoor environments and it is particularly effective in constructing areas containing fine geometries that do not obey multi-view color consistency.

1. Introduction

3D reconstruction and novel view synthesis for indoor environments are of great interest in the computer vision and graphics communities [1, 10, 13, 16, 18, 19, 26, 27, 52, 56]. They provide fundamental support for applications such as robot perception and navigation, virtual reality, and indoor design. Classical indoor 3D reconstruction methods perform registration and fusion to obtain dense geometry using depth images in an explicit manner where the depth images are obtained either with range sensors like Kinect or inferred from RGB images [7, 9, 12, 15, 17, 28, 37, 48]. However, due to noise and holes in the depth images, complete and accurate indoor geometry is difficult to generate. Additionally, such an explicit representation can often fail to preserve sufficient details due to storage limitations thus making it very difficult to synthesize realistic novel views.

In recent years, coordinate neural networks have been extensively used to describe 3D geometry and appearance due to their powerful implicit and continuous representation capacities [25, 26, 31, 32, 43, 45, 49]. These models take the 3D coordinates as input and output the signed distance value [31, 45, 49], density [26, 27], or occupancy of the scene [25, 32, 43]. Although methods such as *Neus* [45] and *VolSDF* [49] can achieve accurate 3D reconstruction of objects, they do not perform well in indoor scenes containing textureless regions or when the observations are sparse. In such cases, depth images are often introduced to provide additional supervision for network training to improve performances [1, 44, 52]. Furthermore, these methods focus on 3D reconstruction and their performances on novel view synthesis can be unsatisfactory.

Neural Radiance Field (NeRF) [26] and a series of its extensions [3, 4, 6, 8, 11, 18, 20, 23, 27, 40, 46, 50, 53–55] have achieved exciting results in novel view synthesis. It implicitly represents the density field and color field and performs novel view synthesis via volume rendering. However, these methods can fail to reconstruct clean indoor surface as the density used in NeRF samples the whole space rather than in the vicinity of the surfaces.

In this paper, we propose a dual neural radiance field (Du-NeRF) to simultaneously achieve high-quality geometry reconstruction and view rendering. Specifically, our framework contains two geometric fields, one is derived from the SDF field with clear boundary definitions, and the other is a density field that is more conducive to rendering. They share the same underlying input features, which are interpolated from multi-resolution feature grids and then decoded by different decoders. Finally, we enable the two

[*] Github: https://github.com/pcl3dv/DuNeRF

[†] Corresponding authors

branches to each play their respective strength, while the former is used to extract geometric features, the latter is used to support the task of new view synthesis. In addition, we decouple a view-independent component from the density field and use it as a label to supervise the learning process of SDF during the network optimization process. In our method, the two geometric fields share the underlying input geometric features to facilitate the optimization of the underlying geometric feature grid. Moreover, we use a view-invariant component decoupled from the density branch to replace the view-varying ground truth (GT) images to guide the geometric learning process to reduce shape-radiance ambiguity and allow geometry and color to benefit from each other during the learning process. Experimental results show that this design can effectively construct fine geometries to achieve smooth scene reconstruction, especially in those areas that do not obey multi-view color consistency. Our contributions are as follows:

- We have developed a novel neural radiance field termed Dual Neural Radiance Field (Du-NeRF) for simultaneously improving 3D reconstruction and new view synthesis of indoor environments.
- We introduce a new self-supervised method to derive a view-independent color component that effectively contributes to filling missing parts in 3D reconstruction.
- Extensive experiments demonstrate that our method can significantly improve the performance of novel view synthesis and 3D reconstruction for indoor environments.

2. Related Work

Neural radiance-based novel view synthesis. The introduction of the neural radiance field (NeRF) marks remarkable progress in novel view generation [26]. NeRF models a full-space implicit differentiable and continuous radiance field with neural networks and uses volume rendering to obtain color information. Many variants have been proposed to improve training, inferencing and rendering performances [3, 4, 6, 8, 20, 23, 27, 40, 46, 54]. In particular, *DirectVoxelGO* [40] and *InstantNGP* [27] combine explicit and implicit representations and use hybrid grid representations and shallow neural networks for density and color estimation respectively to achieve faster rendering speed and higher rendering quality. Liu *et al*. [23] introduce a progressive voxel pruning and growing strategy to sample the effective region near the scene surface. Chen *et al*. [6] use a combination of 2D planes and 1D lines to approximate the grid to achieve faster reconstruction, improved rendering quality, and smaller model sizes. To address the ambiguity arising from pixels represented by a single ray, Barron *et al*. [3] introduce the concept of cones instead of points, to increase the receptive field of a single ray. This approach, known as *Mip-nerf*, effectively tackles issues of jaggies and aliasing and enhances rendering quality. To reduce the blurring effect, Lee *et al*. design a rigid blurry kernel module which takes into account both motion blur and defocus blur during the real acquisition process. Kun *et al*. further improve the rendering performance by learning a degradation-driven inter-viewpoint mixer [54]. Additionally, some works attempt to improve the rendering performance by jointly optimizing the poses of the training images [4, 8, 46]. In contrast, our method adopts geometry-guided sampling, which benefits from the reconstruction result and allows for more accurate sampling of points near the surface, thus improving the performance of view synthesis.

Neural implicit 3D reconstruction. Neural implicit functions take a 3D location as input and output occupancy, density, and color [25, 26, 29, 30, 32]. *Scene Representation Networks* employ MLPs to map 3D coordinates to latent features that encode geometry and color information [38]. Yariv *et al*. [49] and Wang *et al*. [45] propose two approaches to converting SDF values into density and performing volume rendering to supervise object reconstruction in the Nerf-based framework. *Neuralangelo* [22] introduces numerical gradients and utilizes multiresolution hash grids to reconstruct detailed scenes. However, while these methods perform well on scenes with rich texture, they struggle with indoor scenes with textureless walls and ceilings. To address these issues, Yu *et al*. [52] employ predicted depth and normal maps from a pre-trained network to enhance the reconstruction of indoor scenes. Azinović *et al*. [1] combine a TSDF representation with the NeRF framework and use a depth representation from an off-the-shelf RGBD sensor to improve the accuracy of indoor geometry reconstruction. Subsequent studies [21, 44, 47] have further optimized the Neural-RGBD strategy to speed up training. [44] utilizes voxel representations instead of 3D coordinates to achieve faster query, while [47] trains a dynamically adaptive grid that allocates more voxel resources to more complex objects. [21] pre-trains a feature grid to accelerate the training process. We propose to decouple the view-independent colour component for guiding the 3D reconstruction, which effectively fills in the missing parts of depth-based reconstruction.

3. Method

3.1. Preliminaries

Neural radiance field. Given a collection of posed images, neural radiance field can estimate the color and depth of each pixel by computing the weighted sum of sampling points based on their color and distance from the center of the camera [24]:

$$C_p = \sum_{i=1}^{N} w_i c_i, D_p = \sum_{i=1}^{N} w_i z_i, \tag{1}$$

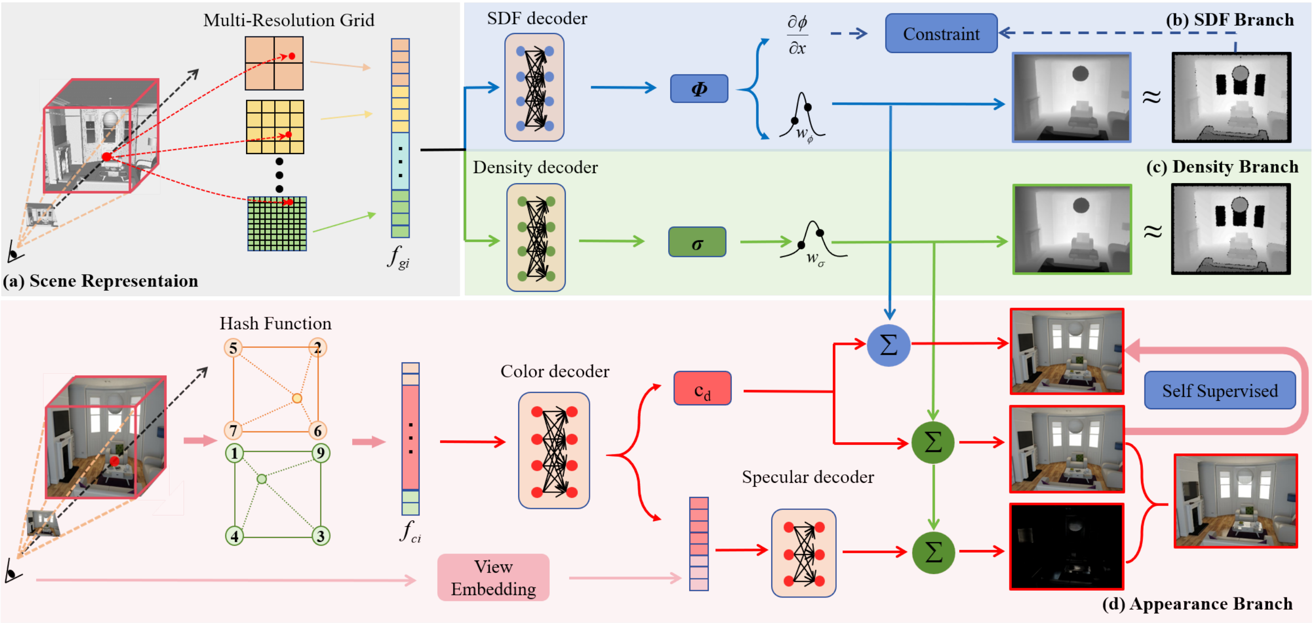

Figure 1. **Du**al **Ne**ural **R**adiance **F**ield (**Du-NeRF**). In (a) Scene Representation, we use a four-layer multi-resolution grid to store geometric features f_{gi}, and a hash-based multi-resolution grid for the color features f_{ci} . f_{gi} is decoded to SDF ϕ and density σ by different MLPs in (b) SDF branch and (c) the Density branch. We provide depth constraints for ϕ and introduce additional regularization terms to ensure the stability of its training. We design a depth alignment loss for σ to align the two geometry fields. In (d), for color calculation, ϕ and σ from (b) and (c) are integrated with decoupled view-independent colors to compute the self-supervised loss. The final rendering color sums the view-dependent and view-independent colors to be integrated with the σ weights.

where the color and distance from sampling points to the camera center, are denoted by c_i and z_i respectively, w_i are the contribution weights of each sampling point to the color and depth and is calculated as $w_i = \sum_i^N (\prod_j^{i-1}(1 - \alpha_j(p(x))))\alpha_i(p(x_i))$, where $p(x)$ and α_i are the density and opacity of sampling point x_i, respectively. The opacity is then computed using Eq. (2).

$$\alpha_i = 1 - exp(-p(x_i)(z_{i+1} - z_i)), \tag{2}$$

the color c_i and density $p(x_i)$ of a given sampling point are predicted by the Multi-layer Perceptron (MLP). The process is illustrated in Eq. (3).

$$p(x_i), f = \Gamma_\theta(x_i), c_i = \Gamma_\kappa(f, d), \tag{3}$$

where x and d represent the location and ray direction, respectively. f is the feature vector related to the location. Γ_θ and Γ_κ are implicit functions modelled by MLPs.

SDF-based neural implicit reconstruction. The signed distance function (SDF) refers to the nearest distance between a point and surfaces and is often used to implicitly represent geometry. One notable application of SDF is neural implicit reconstruction under the volume rendering framework, achieved by a method called Neus [45].

The key to the success of this method is an unbiased transformation between the SDF values and the density, as demonstrated in Eq. (4). This transformation enables the creation of high-quality surface geometry with great accuracy and cleanliness.

$$\alpha_i = \max\left(\frac{\sigma_s\left(\phi\left(\mathbf{x}_i\right)\right) - \sigma_s\left(\phi\left(\mathbf{x}_{i+1}\right)\right)}{\sigma_s\left(\phi\left(\mathbf{x}_i\right)\right)}, 0\right), \tag{4}$$

where $\phi(x_i)$ represents the SDF value of a given sample point, and $\sigma_s(x) = (1 + e^{-sx})^{-1}$, while the smoothness of the surface is conditioned on a learnable parameter s.

Multi-resolution feature grid. To improve the efficiency of training, a grid representation is used [6, 40, 50]. However, using only single-resolution grid limits the optimization of density and color to local information, resulting in disruptions to the smoothness and continuity of the scene texture [44, 52]. A multi-resolution grid expands the local optimization to nearby continuous fields by varying the receptive field and gradient backpropagation of sample points, enabling higher rendering quality and smoother geometry. The embedding feature is obtained by concatenating the features of each level, as shown in Eq. (5).

$$f = \Omega(V_1(x), V_2(x), ..., V_n(x)), \tag{5}$$

where Ω indicates concatenation, and $V_i(x)$ is trilinear interpolation in the i-th grid. The final feature vector of the input network is denoted as f.

To achieve a higher resolution, hash-based feature grid is employed in [27]. It represents resolutions as:

$$R_l := \left\lfloor R_{\min} b^l \right\rfloor,\ b := \exp(\frac{\ln R_{\max} - \ln R_{\max}}{L-1}), \quad (6)$$

where $R_{\min}$, $R_{\max}$ are the coarsest and finest resolution, respectively. R_l represents $l-$th level resolution and L is the total levels. Similarly, we extract the interpolated features at each level and concatenate them together as in Eq. (5).

3.2. Dual Neural Radiance Field

Scene representation. To achieve high-fidelity indoor scene reconstruction and rendering simultaneously, we introduce the dual neural radiance field. The key idea that enables the dual neural radiance field to achieve high-fidelity reconstruction and rendering is to separately represent the geometry field and the color field. Taking into account the fact that the reconstruction task and the rendering task have different complexities, the geometry field and the color field are represented by multi-resolution grids with different levels to speed up training and inference.

As shown in Fig. 1, we use a four-level grid to represent the scene geometry where the grid sizes at each level are respectively 3cm, 6cm, 24cm, and 96cm. At each level, the dimension of the geometry feature is set to 4, and the dimension of the geometry feature f_{gi} is therefore 16. For the color field, the hash-based multi-resolution grid is utilized. The coarsest resolution $R_{\min}$ of the hash-based multi-resolution grid is set to 16. The level of grid resolution is $L = 16$, and the feature vector at each level is 2-dimensional, we therefore obtain a hash color feature vector f_{ci} with a total of 32 dimensions. The geometry feature f_{gi} and color feature f_{ci} are obtained using tri-linear interpolation.

Dual neural radiance networks. The key idea is to use two different geometric decoders to extract SDF and density, which are respectively used for 3D reconstruction and image rendering. The SDF and density are estimated implicitly from the same interpolated features f_{gi}:

$$\Gamma_\phi(f_{gi}) = \phi_i,\ \Gamma_\sigma(f_{gi}) = \sigma_i, \quad (7)$$

where both of the Γ_ϕ and Γ_σ are MLPs, and used to decode f_{gi} into SDF ϕ_i and density σ_i, respectively. ϕ_i and σ_i are both converted to occupancy through Eq. (4) and Eq. (2), respectively. The resulting occupancy of the two is calculated via Eq. (1) to obtain the pixel depth and color. The whole process is supervised with the image reconstruction loss and depth loss.

Sampling points near around object surface have a higher contribution to the rendered color of the ray [26, 45]. To obtain higher rendering quality, we employ the hierarchical sampling strategy as in [26, 45], which contains coarse sampling and fine sampling near the surface. Specifically, we first uniformly sample 96 points along the ray in the coarse stage and then iteratively add 12 sampling points three times according to the cumulative distribution function(CDF) of previous coarse points weights in the fine stage as in [44]. Finally, we got 132 sampling points for depth and color rendering. Note that we use the weight distribution calculated from the SDF branch for sampling as it provides more accurate surface information. For the volume rendering process, the two branches share the sampling points.

Self-supervised color decomposition. We disentangle the color into view-independent color and view-dependent color. We use the decoupled view-independent color c_{di} to guide geometry learning in a multi-view consistent self-supervised manner by constraining the weight values. This separation allows the color branch to leverage complete color information for rendering, while the geometry branch benefits from view-consistent supervision. Previous work has shown that decoupling colors helps mitigate shape-radiance ambiguity [42, 55]. [42] accomplished the color decomposition supervised by the complete color. In contrast, we not only exploit the complete color to supervise the color decomposition but the view-independent color consistency obtained from the SDF branch and density branch in a self-supervised manner. This design effectively extracts view-independent color to support accurate geometry reconstruction but also boosts the image rendering without any additional specular regularity term as in [33, 42].

To achieve it, as shown in Fig. 1, we utilize two color decoders consisting of MLPs to implicitly estimate the view-independent color and view-dependent color. The view-independent decoder takes the interpolated color feature f_{ci} as input and outputs the view-independent color c_{di} and an intermediate feature f_{ini}. The specular (view-dependent) decoder takes the intermediate feature f_{ini} and encodes the view vector as input to obtain the specular color c_{si}. The overall color at a sampling point is calculated by adding the two color components $c_i = c_{di} + c_{si}$. The final color C is generated by summing the weighted color of each sampling point with Eq. (1). In our framework, we integrate ω_{σ_i} with the full color c_i as in *NeRF*, however, we only weight the view-independent color c_{di} with ω_{ϕ_i} to obtain the view-independent color of the corresponding ray. The calculation of color in Eq. (1) becomes:

$$C_{d\phi} = \sum_{i=1}^{N} \omega_{\phi i} c_{di}, \quad (8)$$

where $C_{d\phi}$ is the view-independent color computed by $\omega_{\phi i}$. We can obtain the view-independent color $C_{d\sigma}$ computed by c_{di} and ω_{σ_i}, which will be used as the ground truth to constrain the learning process of $C_{d\phi}$:

$$\mathcal{L}_d = \sum_{i}^{N} \lambda_d \left\| C_{d\phi} - C_{d\sigma} \right\|. \quad (9)$$

3.3. Network training

To optimize the dual neural radiance field, we randomly sample M rays during training. Our loss is divided into two components including a $\mathcal{L}_\phi$ loss, and a $\mathcal{L}_\sigma$ loss in Eq. (10).

$$\mathcal{L}(\mathrm{P}) = \mathcal{L}_\phi + \mathcal{L}_\sigma. \tag{10}$$

The $\mathcal{L}_\phi$ contains the three components as shown in Eq. (11): view-independent color loss, depth loss and SDF regularization loss, as the following:

$$\mathcal{L}_\phi = \lambda_d \mathcal{L}_d + \lambda_{\text{depth}} \mathcal{L}_{\text{depth}} + \mathcal{L}_{\text{SDF}}. \tag{11}$$

The view-independent loss is calculated as the distance between $C_{d\phi}$ and $C_{d\sigma}$ as shown in Eq. (9), and the depth loss is the L_1 loss:

$$\mathcal{L}_{\text{depth}} = \sum_i^N |D_\phi - D_{\text{gt}}| \,. \tag{12}$$

In order to improve the robustness of the learning process of the SDF ϕ, we imposed a series of SDF losses $\mathcal{L}_{\text{SDF}}$ to regularize the ϕ value as [44]:

$$\mathcal{L}_{\text{SDF}} = \lambda_{\text{eik}} \mathcal{L}_{\text{eik}} + \lambda_{\text{fs}} \mathcal{L}_{\text{fs}} + \lambda_{\text{sdf}} \mathcal{L}_{\text{sdf}} + \lambda_{\text{smooth}} \mathcal{L}_{\text{smooth}} \,. \tag{13}$$

The regularization term $\mathcal{L}_{\text{eik}}(x)$ encourages valid SDF predictions in the unsupervised regions, while $\mathcal{L}_{\text{smooth}}(x)$ is an explicit smoothness term to realize smooth surfaces.

$$\mathcal{L}_{\text{eik}}(x) = (1 - \|\nabla \phi(x)\|)^2, \tag{14}$$

$$\mathcal{L}_{\text{smooth}}(x) = \|\nabla \phi(x) - \nabla \phi(x + \epsilon)\|^2. \tag{15}$$

$\mathcal{L}_{\text{sdf}}(x)$ and $\mathcal{L}_{\text{fs}}(x)$ are used to constrain the truncation distance $b(x)$.

$$\mathcal{L}_{\text{sdf}}(x) = |\phi(x) - b(x)|, \tag{16}$$

$$\mathcal{L}_{\text{fs}}(x) = \max\left(0, e^{-\alpha\phi(x)} - 1, \phi(x) - b(x)\right). \tag{17}$$

A detailed explanation of these regularity constraints can be found in [44].

The $\mathcal{L}_\sigma$ loss contains two parts as shown in Eq. (18):

$$\mathcal{L}_\sigma = \lambda_{\text{rgb}} \sum_i^N \|C_\sigma - C_{\text{gt}}\| + \lambda_{\text{align}} \sum_i^N |D_\sigma - D_{\text{gt}}| \,, \tag{18}$$

where C_σ is the final rendering color and D_σ is the depth calculated from the color branch. λ_{align} is used to align two geometric fields. We experimentally found that $\mathcal{L}_{\text{align}}$ is important for decoupling consistent view-independent color. For each of the geometry coefficients, we follow the practice of [44] and set them as follows: $\lambda_d = 5$, $\lambda_{\text{depth}} = 1$, $\lambda_{\text{eik}} = 1.0$, $\lambda_{\text{fs}} = 1.0$, $\lambda_{\text{sdf}} = 10.0$, $\lambda_{\text{smooth}} = 1.0$. For color coefficients we experimentally set them as $\lambda_{\text{rgb}} = 50$ and $\lambda_{\text{align}} = 1$.

4. Experiment

4.1. Setup

Implementation details. The SDF decoder Γ_ϕ, density decoder Γ_σ, color decoder Γ_d and specular decoder Γ_s all use two-layers MLPs with the hidden dimension of 32. We sample $M = 6144$ rays for each iteration, each ray contains $N_c = 96$ coarse samples and $N_f = 36$ fine samples. Our method is implemented in Pytorch and trained with the ADAM optimizer with a learning rate of 1×10^{-3}, and 1×10^{-2} for MLP decoders, multi-resolution grids features, respectively. We run 20K iterations in all scenes with the learning rate decay at iteration 10000 and 15000, and the decay rate is $1/3$.

Baselines. To validate the effectiveness of the proposed method, we compare it with approaches to indoor 3D reconstruction and view rendering, respectively. For indoor 3D reconstruction, we compare with registration-based method including *BundleFusion* [10], *Colmap* [34–36], *Convolutional Occupancy Networks* [32], *SIREN* [39], and recent volumetric rendering-based geometry reconstruction methods such as *Neus* [45], *VolSDF* [49], *Neural RGBD* [1], and *Go-Surf* [44]. We run marching cubes at the resolution of 1cm to extract meshes. We cull the points and faces in the areas that are not observed in any camera views as in [1, 44]. Besides, the same pose refinement is applied in the same way as in [1, 44].

For image rendering, we compare some representative approaches based on the neural radiance field, including *DVGO* [40] and *InstantNGP* [27]. We extract their mesh structures by marching cubes, and compare their geometric metrics and rendering quality. We implement these methods based on *SDFstudio* [51] and *NeRFstudio* [41].

4.2. Comparison

Evaluation on NeuralRGBD Dataset. We evaluated our method on 10 synthesis data used in *NeuralRGBD* and *Go-Surf*. The NeuralRGBD dataset consists of 10 synthetic scenes. It provides images, corresponding poses from the Bundlefusion algorithm, and noised depths. The noised depth is used to simulate the collection of real depth sensor Kinect. To compare the image synthesis performance, we choose about 10% of the images as the validation set for image rendering comparison. Specifically, we chose one image from every 10 images of the image sequence as the validation dataset. The first and last images were discarded to avoid the interference of marginal areas that can not observed by the training dataset.

Qualitative and quantitative results are shown in Fig. 2 and Tab. 1. It can be seen from Tab. 1 that our method obtains the best performance on image rendering and indoor reconstruction compared with previous approaches. Specifically, we achieve the best performances in accuracy, com-

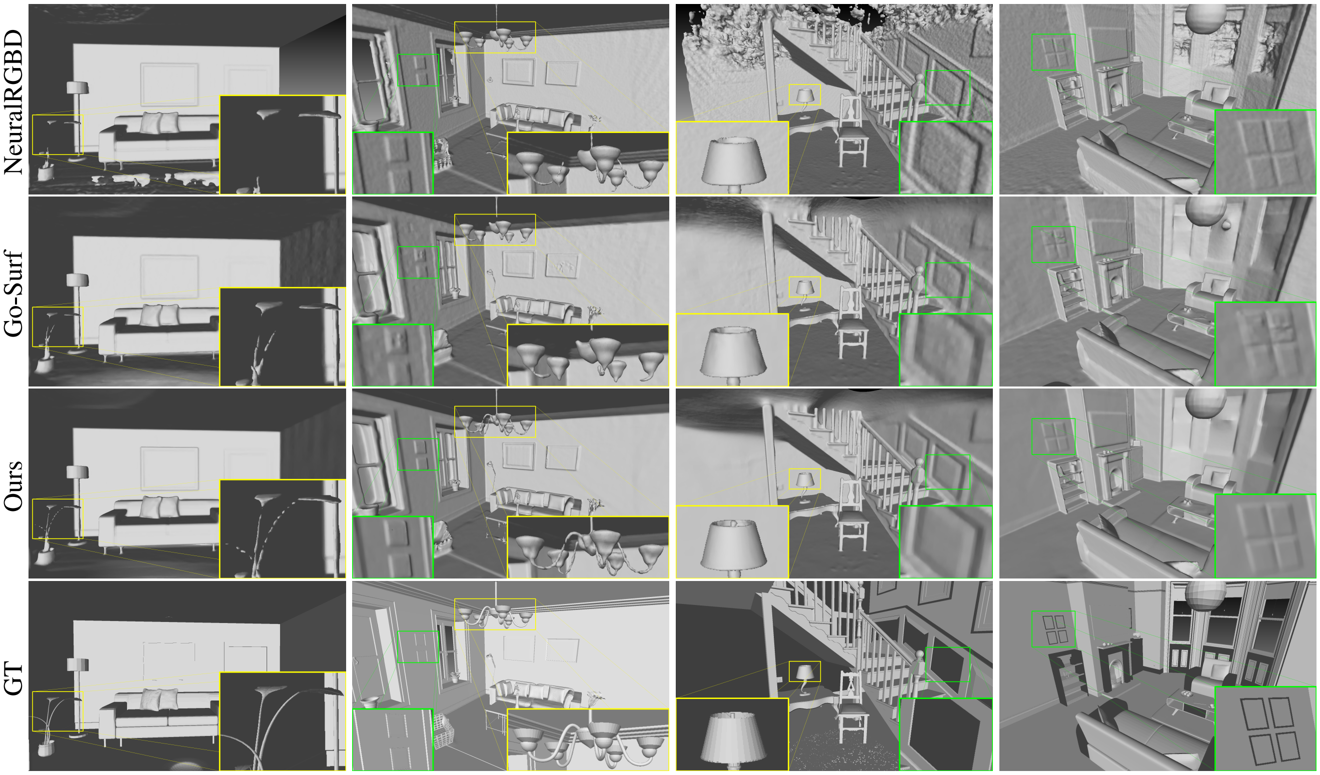

Figure 2. The qualitative reconstruction results on NeuralRGB datasets. The proposed method can fill in the missing part (highlighted in yellow boxes) and produce smoother planes and clear edges (highlighted in green boxes)

Method	Acc ↓	Com ↓	C-l_1 ↓	NC ↑	F-score ↑	PSNR ↑	SSIM ↑	LPIPS ↓
BundleFusion	0.0178	0.4577	0.2378	0.851	0.680	-	-	-
COLMAP	0.0271	0.0364	0.0293	0.888	0.874	-	-	-
ConvOccNets	0.0498	0.0524	0.0511	0.861	0.682	-	-	-
SIREN	0.0229	0.0412	0.0320	0.905	0.852	-	-	-
Neus	0.3174	0.6911	0.5043	0.628	0.103	27.465	0.849	0.192
VolSDF	0.1627	0.4815	0.3222	0.681	0.262	28.717	0.882	0.174
Neural RGB-D	**0.0145**	0.0508	0.0327	0.920	0.936	31.994	0.901	0.183
Go-Surf	0.0164	0.0213	0.0189	0.932	0.949	29.586	0.889	0.183
DVGO	0.2389	0.5558	0.3973	0.564	0.317	33.633	0.940	0.125
Instant-NGP	0.2641	0.7318	0.4976	0.555	0.208	27.976	0.799	0.255
Ours	0.0156	**0.0197**	**0.0177**	**0.933**	**0.960**	**36.503**	**0.966**	**0.048**

Table 1. Reconstruction and view synthesis results of Neural-RGBD dataset. The best performances are highlighted in bold.

pletion, chamfer l_1 distance, and the highest F-score values. We also achieve the highest PSNR and SSIM and the lowest LPIPS. Additionally, Fig. 2 shows that our approach can fill in the missing parts of the scene in scene reconstruction, such as the legs of the chair and light strips. We also obtain smoother surfaces in flat areas such as the floor. In terms of view rendering, our approach exceeds rendering and reconstruction of previous approaches in reconstructing geometric features and achieves visually better images.

Evaluation on Replica dataset. The Replica dataset consists of 18 scenes, which are closer to real-world scenes. Each scene contains about 2000 high-quality images and depth images. We also add noise to their depth images, as in [1], to simulate real depth images [2, 5, 14]. Moreover, we also perform BundleFusion to produce the camera poses. We chose one image from every 10 images for the whole image sequence as the validation dataset. We empirically discard the first and last images as they capture scenes that the training dataset does not have.

It can be seen from table Tab. 2 that our method achieves the best performance on geometry reconstruction and view rendering. Specifically, for geometric reconstruction, the proposed method achieves better performance than traditional BundleFusion in all metrics. Moreover, we achieve higher F-score and lower chamfer-l_1 compared to *Neural-RGBD* and *Go-Surf*. In terms of view rendering, our method outperforms these methods by a large margin in all three metrics, even better than DVGO and Instant-NGP, which are designed for novel view synthesis. Qualitative results can be found in the supplementary material.

Complexity and efficiency. The proposed method takes about 50 to 90 minutes on our hardware to obtain a high-quality rendering and reconstruction. This performance is slower than *Go-Surf* [44] (15-45 minutes) but way faster than *Neural RGBD* [1] (over 12 hours). The storage requirement of Du-NeRF is comparable to that of *Go-surf* which is

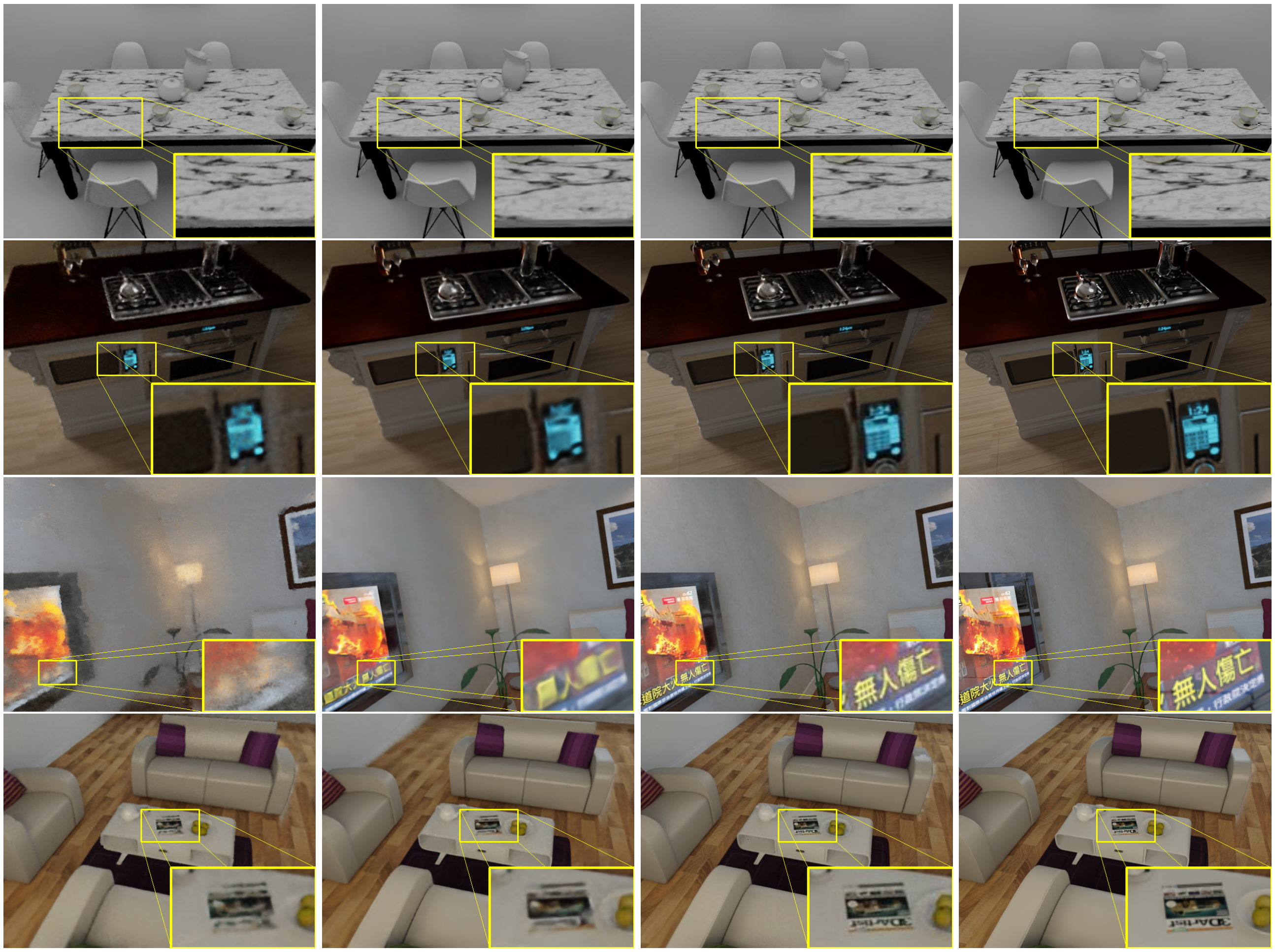

(a) InstantNGP (b) DVGO (c) Ours (d) GT

Figure 3. Qualitative comparison of novel view synthesis results of NeuralRGBD dataset. It can be seen from the results that our method has better visual rendering effects, whether they are striped structures or text on books.

Method	**Acc** ↓	**Com** ↓	**C-l_1** ↓	**NC** ↑	**F-score** ↑	**PSNR** ↑	**SSIM** ↑	**LPIPS** ↓
BundleFusion	0.0145	0.0453	0.0299	0.961	0.936	-	-	-
Neus	0.1623	0.2956	0.2288	0.754	0.194	28.939	0.855	0.181
VolSDF	0.1348	0.3009	0.2180	0.747	0.339	30.375	0.866	0.175
Neural RGB-D	**0.0096**	0.2447	0.1271	0.934	0.847	32.668	0.893	0.198
Go-Surf	0.0120	0.0122	0.0121	0.9718	0.9896	30.967	0.884	0.217
DVGO	0.2399	0.3511	0.2955	0.6040	0.239	31.962	0.893	0.223
Instant-NGP	0.3332	1.1151	0.7288	0.5470	0.1583	32.352	0.884	0.150
Ours	0.0112	**0.0111**	**0.0112**	**0.9748**	**0.9911**	**37.104**	**0.955**	**0.074**

Table 2. Reconstruction and view synthesis results of Replica dataset. The best performances are highlighted in bold.

in the order of hundreds of MB for storing two feature grids and other network parameters.

4.3. Ablations

We conduct ablation studies to demonstrate the effectiveness of designing the blocks and choice of scene representation. The quantitative result is shown in Tabs. 3 to 5, where we evaluate these methods in the RGBD synthetic dataset.

Effect of the Du-NeRF architecture. As shown in Tab. 3, the dual field significantly improves the view rendering performance, and simultaneously increases reconstruction performance. The SDF-only in Tab. 3 means only the SDF branch used for neural volume rendering without the density branch, while the Density-only represents only the density branch without that of SDF. Dual field means that two branches are used for volume rendering at the same time, in which the final color comes from the density branch, and the geometry is extracted from the SDF branch. This demonstrates the effectiveness of the proposed dual-field structure in enhancing the view rendering and indoor 3D reconstruction.

Effect of color disentanglement. Tab. 4 shows the ablation experiments of the color disentanglement (C-D). We tested the impact of different components of the color decoupling process on the final result, including the view-

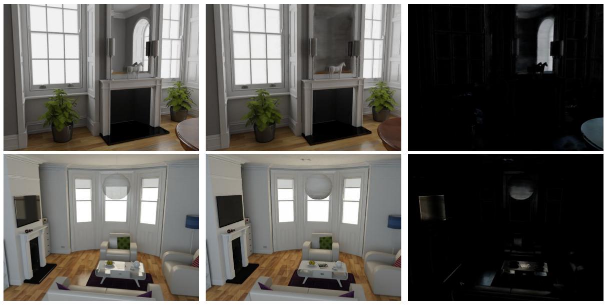

(a) Complete color (b) Vi color (c) Vd color

Figure 4. Color decoupling results of the proposed method on NeuralRGBD dataset. The Vi color represents the view-independent color, while Vd color is the view-dependent color. It can be seen that our method can effectively decouple the complete color into the view-dependent (specular reflective surfaces) and view-independent (diffusion surfaces) colors.

Method	**C-l_1 ↓**	**F-score ↑**	**PSNR ↑**	**LPIPS ↓**
SDF-only	0.0203	0.9500	32.198	0.117
Density-only	0.0279	0.8798	31.681	0.155
Dual(SDF+Density)	**0.0182**	**0.9549**	**34.494**	**0.090**

Table 3. Ablation study of the dual branches. Compared to the single SDF-branch and Density-branch, the dual branches achieve the best results of both reconstruction and rendering.

independent component (ViC), view-dependent component (VdC), and complete color (FC) is the sum of VdC and ViC. For the first row we use Fc instead of VdC+ViC due to color decoupling is not used in this experiment. It can be seen from the results that pure color decoupling cannot improve the quality of reconstruction and rendering from the first two rows. In addition, using ViC supervision to guide the learning of the SDF branch, the performance on F-score and PSNR are higher than other ways of supervision and the method without C-D, which confirms the effectiveness of our approach discussed in Sec. 3.2. The color decomposition results are shown in Fig. 4. It can be seen that the proposed method successfully decomposes the view-dependent color and view-independent color (see regions in the mirror, the reflective books, and the desk).

Effect of different grid representation. In Tab. 5, $\mathrm{G_M} - \mathrm{C_M}$ indicates the geometry and colour are both represented with four-level resolution grids, $\mathrm{G_H} - \mathrm{C_H}$ indicates the two are hash-based grid, and $\mathrm{G_M} - \mathrm{C_H}$ denotes the geometry is represented with a four-level grid while color is a hash-based grid. Tab. 5 shows that the hash representation of color features is helpful for obtaining better rendering performances while the hash representation of geometry features severely decreases the reconstruction quality.

C-D	**Supervised**	**C-l_1 ↓**	**F-score ↑**	**PSNR ↑**	**LPIPS ↓**
w/o	FC	0.0182	0.9549	34.494	0.090
w/	VdC+ViC	0.0185	0.9526	34.710	0.080
w/	VdC	0.1658	0.6503	32.780	0.122
w/	ViC	**0.0177**	**0.9597**	**35.225**	**0.072**

Table 4. Ablation study of color disentanglement (C-D) on reconstruction and novel view synthesis. Tab. 4 shows the effect of different color for SDF supervision on the reconstruction and novel view synthesis results after color decoupling. ViC (Ours) denotes the view-independent component, VdC is the view-dependent component, and FC represents the complete color. Experimental results demonstrate that supervised by the view-independent color component gives the best performance on reconstruction and rendering.

Method	**C-l_1 ↓**	**F-score ↑**	**PSNR ↑**	**LPIPS ↓**
$\mathrm{G_M} - \mathrm{C_M}$	**0.0177**	0.9597	35.225	0.072
$\mathrm{G_H} - \mathrm{C_H}$	0.0294	0.8976	36.087	0.108
$\mathbf{G_M} - \mathbf{C_H}$	**0.0177**	**0.9600**	**36.503**	**0.048**

Table 5. Evaluation of different scene representation, where $\mathrm{G_M}$, $\mathrm{C_M}$, $\mathrm{G_H}$, $\mathrm{C_H}$, denote geometric multi-resolution grid, color multi-resolution grid, geometric hash grid, and color hash grid, respectively. It can be seen that a four-level multi-resolution grid has better geometry representation and a hash-based multi-resolution grid gives better image rendering performance.

5. Concluding remarks

We have presented a dual neural radiance field for high-fidelity 3D scene reconstruction and rendering simultaneously. By designing two branches for reconstruction and view rendering respectively, the proposed method allows the two tasks to benefit from each other. To further improve the reconstruction and rendering performances, we designed a self-supervised color decomposition method. Experimental results have shown that our self-supervised method simultaneously improves the geometric reconstruction and rendering capabilities. Moreover, our method achieves state-of-the-art performances compared to previous methods.

Limitation and future work. Although Du-NeRF has been experimentally proven to be effective, our method may perform poorly if the observed images are blurred because it relies on multi-view color consistency to supervise geometry reconstruction and blur images do not satisfy such requirements. Besides, the effectiveness of the proposed method remains to be tested under a few-shot scenario where a small number of RGBD images are provided. In addition, trying new feature representations such as replacing hash representation with Gaussian splitting may improve performances. We will address these in future works.

References

[1] Dejan Azinović, Ricardo Martin-Brualla, Dan B Goldman, Matthias Nießner, and Justus Thies. Neural rgb-d surface reconstruction. In *Proceedings of the IEEE/CVF Conference on Computer Vision and Pattern Recognition*, pages 6290–6301, 2022. 1, 2, 5, 6

[2] Jonathan T Barron and Jitendra Malik. Intrinsic scene properties from a single rgb-d image. In *Proceedings of the IEEE Conference on Computer Vision and Pattern Recognition*, pages 17–24, 2013. 6, 1

[3] Jonathan T Barron, Ben Mildenhall, Matthew Tancik, Peter Hedman, Ricardo Martin-Brualla, and Pratul P Srinivasan. Mip-nerf: A multiscale representation for anti-aliasing neural radiance fields. In *Proceedings of the IEEE/CVF International Conference on Computer Vision*, pages 5855–5864, 2021. 1, 2

[4] Wenjing Bian, Zirui Wang, Kejie Li, Jia-Wang Bian, and Victor Adrian Prisacariu. Nope-nerf: Optimising neural radiance field with no pose prior. In *Proceedings of the IEEE/CVF Conference on Computer Vision and Pattern Recognition*, pages 4160–4169, 2023. 1, 2

[5] Jeannette Bohg, Javier Romero, Alexander Herzog, and Stefan Schaal. Robot arm pose estimation through pixel-wise part classification. In *2014 IEEE International Conference on Robotics and Automation (ICRA)*, pages 3143–3150. IEEE, 2014. 6, 1

[6] Anpei Chen, Zexiang Xu, Andreas Geiger, Jingyi Yu, and Hao Su. Tensorf: Tensorial radiance fields. In *Computer Vision – ECCV 2022*, pages 333–350. 2022. 1, 2, 3

[7] Jiawen Chen, Dennis Bautembach, and Shahram Izadi. Scalable real-time volumetric surface reconstruction. *ACM Transactions on Graphics (ToG)*, 32(4):1–16, 2013. 1

[8] Yu Chen and Gim Hee Lee. Dbarf: Deep bundle-adjusting generalizable neural radiance fields. In *Proceedings of the IEEE/CVF Conference on Computer Vision and Pattern Recognition*, pages 24–34, 2023. 1, 2

[9] Brian Curless and Marc Levoy. A volumetric method for building complex models from range images. In *Proceedings of the 23rd annual conference on Computer graphics and interactive techniques*, pages 303–312, 1996. 1

[10] Angela Dai, Matthias Nießner, Michael Zollhöfer, Shahram Izadi, and Christian Theobalt. Bundlefusion: Real-time globally consistent 3d reconstruction using on-the-fly surface reintegration. *ACM Transactions on Graphics (ToG)*, 36(4): 1, 2017. 1, 5

[11] Sara Fridovich-Keil, Alex Yu, Matthew Tancik, Qinhong Chen, Benjamin Recht, and Angjoo Kanazawa. Plenoxels: Radiance fields without neural networks. In *Proceedings of the IEEE/CVF Conference on Computer Vision and Pattern Recognition*, pages 5501–5510, 2022. 1

[12] Clément Godard, Oisin Mac Aodha, and Gabriel J Brostow. Unsupervised monocular depth estimation with left-right consistency. In *Proceedings of the IEEE conference on computer vision and pattern recognition*, pages 270–279, 2017. 1

[13] Haoyu Guo, Sida Peng, Haotong Lin, Qianqian Wang, Guofeng Zhang, Hujun Bao, and Xiaowei Zhou. Neural 3d scene reconstruction with the manhattan-world assumption. In *Proceedings of the IEEE/CVF Conference on Computer Vision and Pattern Recognition*, pages 5511–5520, 2022. 1

[14] Ankur Handa, Thomas Whelan, John McDonald, and Andrew J Davison. A benchmark for rgb-d visual odometry, 3d reconstruction and slam. In *2014 IEEE international conference on Robotics and automation (ICRA)*, pages 1524–1531. IEEE, 2014. 6, 1

[15] Shahram Izadi, David Kim, Otmar Hilliges, David Molyneaux, Richard Newcombe, Pushmeet Kohli, Jamie Shotton, Steve Hodges, Dustin Freeman, Andrew Davison, et al. Kinectfusion: real-time 3d reconstruction and interaction using a moving depth camera. In *Proceedings of the 24th annual ACM symposium on User interface software and technology*, pages 559–568, 2011. 1

[16] Xujie Kang, Kanglin Liu, Jiang Duan, Yuanhao Gong, and Guoping Qiu. P2i-net: Mapping camera pose to image via adversarial learning for new view synthesis in real indoor environments. page 2635–2643, 2023. 1

[17] Abhishek Kar, Christian Häne, and Jitendra Malik. Learning a multi-view stereo machine. *Advances in neural information processing systems*, 30, 2017. 1

[18] Bernhard Kerbl, Georgios Kopanas, Thomas Leimkühler, and George Drettakis. 3d gaussian splatting for real-time radiance field rendering. *ACM Transactions on Graphics (ToG)*, 42(4):1–14, 2023. 1

[19] Obin Kwon, Jeongho Park, and Songhwai Oh. Renderable neural radiance map for visual navigation. In *Proceedings of the IEEE/CVF Conference on Computer Vision and Pattern Recognition*, pages 9099–9108, 2023. 1

[20] Dogyoon Lee, Minhyeok Lee, Chajin Shin, and Sangyoun Lee. Dp-nerf: Deblurred neural radiance field with physical scene priors. In *Proceedings of the IEEE/CVF Conference on Computer Vision and Pattern Recognition*, pages 12386–12396, 2023. 1, 2

[21] Seunghwan Lee, Gwanmo Park, Hyewon Son, Jiwon Ryu, and Han Joo Chae. Fastsurf: Fast neural rgb-d surface reconstruction using per-frame intrinsic refinement and tsdf fusion prior learning. *arXiv preprint arXiv:2303.04508*, 2023. 2

[22] Zhaoshuo Li, Thomas Müller, Alex Evans, Russell H Taylor, Mathias Unberath, Ming-Yu Liu, and Chen-Hsuan Lin. Neuralangelo: High-fidelity neural surface reconstruction. In *Proceedings of the IEEE/CVF Conference on Computer Vision and Pattern Recognition*, pages 8456–8465, 2023. 2

[23] Lingjie Liu, Jiatao Gu, Kyaw Zaw Lin, Tat-Seng Chua, and Christian Theobalt. Neural sparse voxel fields. *Advances in Neural Information Processing Systems*, 33:15651–15663, 2020. 1, 2

[24] Nelson Max. Optical models for direct volume rendering. *IEEE Transactions on Visualization and Computer Graphics*, 1(2):99–108, 1995. 2

[25] Lars Mescheder, Michael Oechsle, Michael Niemeyer, Sebastian Nowozin, and Andreas Geiger. Occupancy networks: Learning 3d reconstruction in function space. In *Proceedings of the IEEE/CVF conference on computer vision and pattern recognition*, pages 4460–4470, 2019. 1, 2

[26] B Mildenhall, PP Srinivasan, M Tancik, JT Barron, R Ramamoorthi, and R Ng. Nerf: Representing scenes as neural

radiance fields for view synthesis. In *European conference on computer vision*, 2020. 1, 2, 4

[27] Thomas Müller, Alex Evans, Christoph Schied, and Alexander Keller. Instant neural graphics primitives with a multiresolution hash encoding. *ACM Transactions on Graphics*, 41 (4):1–15, 2022. 1, 2, 4, 5

[28] Matthias Nießner, Michael Zollhöfer, Shahram Izadi, and Marc Stamminger. Real-time 3d reconstruction at scale using voxel hashing. *ACM Transactions on Graphics (ToG)*, 32 (6):1–11, 2013. 1

[29] Michael Oechsle, Lars Mescheder, Michael Niemeyer, Thilo Strauss, and Andreas Geiger. Texture fields: Learning texture representations in function space. In *Proceedings of the IEEE/CVF International Conference on Computer Vision*, pages 4531–4540, 2019. 2

[30] Michael Oechsle, Songyou Peng, and Andreas Geiger. Unisurf: Unifying neural implicit surfaces and radiance fields for multi-view reconstruction. In *Proceedings of the IEEE/CVF International Conference on Computer Vision*, pages 5589–5599, 2021. 2

[31] Jeong Joon Park, Peter Florence, Julian Straub, Richard Newcombe, and Steven Lovegrove. Deepsdf: Learning continuous signed distance functions for shape representation. In *Proceedings of the IEEE/CVF conference on computer vision and pattern recognition*, pages 165–174, 2019. 1

[32] Songyou Peng, Michael Niemeyer, Lars Mescheder, Marc Pollefeys, and Andreas Geiger. Convolutional occupancy networks. In *Computer Vision–ECCV 2020: 16th European Conference, Glasgow, UK, August 23–28, 2020, Proceedings, Part III 16*, pages 523–540. Springer, 2020. 1, 2, 5

[33] Christian Reiser, Rick Szeliski, Dor Verbin, Pratul Srinivasan, Ben Mildenhall, Andreas Geiger, Jon Barron, and Peter Hedman. Merf: Memory-efficient radiance fields for real-time view synthesis in unbounded scenes. *ACM Transactions on Graphics (TOG)*, 42(4):1–12, 2023. 4

[34] Johannes L Schonberger and Jan-Michael Frahm. Structure-from-motion revisited. In *Proceedings of the IEEE conference on computer vision and pattern recognition*, pages 4104–4113, 2016. 5

[35] Johannes L Schönberger, Enliang Zheng, Jan-Michael Frahm, and Marc Pollefeys. Pixelwise view selection for unstructured multi-view stereo. In *Computer Vision–ECCV 2016: 14th European Conference, Amsterdam, The Netherlands, October 11-14, 2016, Proceedings, Part III 14*, pages 501–518. Springer, 2016.

[36] Johannes L Schönberger, True Price, Torsten Sattler, Jan-Michael Frahm, and Marc Pollefeys. A vote-and-verify strategy for fast spatial verification in image retrieval. In *Computer Vision–ACCV 2016: 13th Asian Conference on Computer Vision, Taipei, Taiwan, November 20-24, 2016, Revised Selected Papers, Part I 13*, pages 321–337. Springer, 2017. 5

[37] Vincent Sitzmann, Justus Thies, Felix Heide, Matthias Nießner, Gordon Wetzstein, and Michael Zollhofer. Deepvoxels: Learning persistent 3d feature embeddings. In *Proceedings of the IEEE/CVF Conference on Computer Vision and Pattern Recognition*, pages 2437–2446, 2019. 1

[38] Vincent Sitzmann, Michael Zollhöfer, and Gordon Wetzstein. Scene representation networks: Continuous 3d-structure-aware neural scene representations. *Advances in Neural Information Processing Systems*, 32, 2019. 2

[39] Vincent Sitzmann, Julien Martel, Alexander Bergman, David Lindell, and Gordon Wetzstein. Implicit neural representations with periodic activation functions. *Advances in neural information processing systems*, 33:7462–7473, 2020. 5

[40] Cheng Sun, Min Sun, and Hwann-Tzong Chen. Direct voxel grid optimization: Super-fast convergence for radiance fields reconstruction. In *Proceedings of the IEEE/CVF Conference on Computer Vision and Pattern Recognition*, pages 5459–5469, 2022. 1, 2, 3, 5

[41] Matthew Tancik, Ethan Weber, Evonne Ng, Ruilong Li, Brent Yi, Justin Kerr, Terrance Wang, Alexander Kristoffersen, Jake Austin, Kamyar Salahi, Abhik Ahuja, David McAllister, and Angjoo Kanazawa. Nerfstudio: A modular framework for neural radiance field development. In *ACM SIGGRAPH 2023 Conference Proceedings*, 2023. 5

[42] Jiaxiang Tang, Hang Zhou, Xiaokang Chen, Tianshu Hu, Errui Ding, Jingdong Wang, and Gang Zeng. Delicate textured mesh recovery from nerf via adaptive surface refinement. *arXiv preprint arXiv:2303.02091*, 2023. 4

[43] Maxim Tatarchenko, Alexey Dosovitskiy, and Thomas Brox. Octree generating networks: Efficient convolutional architectures for high-resolution 3d outputs. In *Proceedings of the IEEE international conference on computer vision*, pages 2088–2096, 2017. 1

[44] Jingwen Wang, Tymoteusz Bleja, and Lourdes Agapito. Gosurf: Neural feature grid optimization for fast, high-fidelity rgb-d surface reconstruction. In *2022 International Conference on 3D Vision (3DV)*, pages 433–442. IEEE, 2022. 1, 2, 3, 4, 5, 6

[45] Peng Wang, Lingjie Liu, Yuan Liu, Christian Theobalt, Taku Komura, and Wenping Wang. Neus: Learning neural implicit surfaces by volume rendering for multi-view reconstruction. *arXiv preprint arXiv:2106.10689*, 2021. 1, 2, 3, 4, 5

[46] Peng Wang, Yuan Liu, Zhaoxi Chen, Lingjie Liu, Ziwei Liu, Taku Komura, Christian Theobalt, and Wenping Wang. F2-nerf: Fast neural radiance field training with free camera trajectories. In *Proceedings of the IEEE/CVF Conference on Computer Vision and Pattern Recognition*, pages 4150–4159, 2023. 1, 2

[47] Xiangyu Xu, Lichang Chen, Changjiang Cai, Huangying Zhan, Qingan Yan, Pan Ji, Junsong Yuan, Heng Huang, and Yi Xu. Dynamic voxel grid optimization for high-fidelity rgb-d supervised surface reconstruction. *arXiv preprint arXiv:2304.06178*, 2023. 2

[48] Yao Yao, Zixin Luo, Shiwei Li, Tian Fang, and Long Quan. Mvsnet: Depth inference for unstructured multi-view stereo. In *Proceedings of the European conference on computer vision (ECCV)*, pages 767–783, 2018. 1

[49] Lior Yariv, Jiatao Gu, Yoni Kasten, and Yaron Lipman. Volume rendering of neural implicit surfaces. *Advances in Neural Information Processing Systems*, 34:4805–4815, 2021. 1, 2, 5

[50] Alex Yu, Ruilong Li, Matthew Tancik, Hao Li, Ren Ng, and Angjoo Kanazawa. Plenoctrees for real-time rendering

of neural radiance fields. In *Proceedings of the IEEE/CVF International Conference on Computer Vision*, pages 5752–5761, 2021. 1, 3

[51] Zehao Yu, Anpei Chen, Bozidar Antic, Songyou Peng, Apratim Bhattacharyya, Michael Niemeyer, Siyu Tang, Torsten Sattler, and Andreas Geiger. Sdfstudio: A unified framework for surface reconstruction, 2022. 5

[52] Zehao Yu, Songyou Peng, Michael Niemeyer, Torsten Sattler, and Andreas Geiger. Monosdf: Exploring monocular geometric cues for neural implicit surface reconstruction. *Advances in neural information processing systems*, 35:25018–25032, 2022. 1, 2, 3

[53] Kai Zhang, Gernot Riegler, Noah Snavely, and Vladlen Koltun. Nerf++: Analyzing and improving neural radiance fields. *arXiv preprint arXiv:2010.07492*, 2020. 1

[54] Kun Zhou, Wenbo Li, Yi Wang, Tao Hu, Nianjuan Jiang, Xiaoguang Han, and Jiangbo Lu. Nerflix: High-quality neural view synthesis by learning a degradation-driven interviewpoint mixer. In *Proceedings of the IEEE/CVF Conference on Computer Vision and Pattern Recognition*, pages 12363–12374, 2023. 2

[55] Bingfan Zhu, Yanchao Yang, Xulong Wang, Youyi Zheng, and Leonidas Guibas. Vdn-nerf: Resolving shape-radiance ambiguity via view-dependence normalization. In *Proceedings of the IEEE/CVF Conference on Computer Vision and Pattern Recognition*, pages 35–45, 2023. 1, 4

[56] Michael Zollhöfer, Patrick Stotko, Andreas Görlitz, Christian Theobalt, Matthias Nießner, Reinhard Klein, and Andreas Kolb. State of the art on 3d reconstruction with rgb-d cameras. In *Computer graphics forum*, pages 625–652. Wiley Online Library, 2018. 1

3D Reconstruction and New View Synthesis of Indoor Environments based on a Dual Neural Radiance Field

Supplementary Material

6. Additional Implementation Details

6.1. More details of the dataset

We use the *NeuralRGBD* and the *Replica* datasets to evaluate the proposed method. The *NeuralRGBD* contains ten synthetic scenes and the *Replica* has eight real-world scenes. Each scene consists of RGB images, depth images (coarse, real) and poses (coarse, real).

We use the coarse depth images and poses for all experiments. The coarse depth images are made by adding noise to real depth images to simulate depth images obtained by the real depth sensor as in [2, 5, 14], and the coarse poses are estimated by *BundleFusion* using noisy depth images. For each scene, about 10 percent of images are used as validation sets and the rest of the images are used as training sets. Specifically, starting with the 10-th image, we choose one image in every ten consecutive images as the validation set. The details of the number of datasets are shown in Tab. 6.

Scene	Frames	Train	Validate
Breakfast room	1167	1051	116
Green room	1440	1297	143
Grey-white room	1490	1342	148
ICL living room	1445	1301	144
Complete kitchen	1210	1090	120
Kitchen	1184	1066	118
Morning apartment	920	829	91
Staircase	1118	1007	111
Thin Geometry	395	356	39
White room	1676	1509	167
Office0	2000	1801	199
Office1	2000	1801	199
Office2	1997	1798	199
Office3	1963	1767	196
Office4	1968	1772	196
Room0	1985	1787	198
Room1	1996	1797	199
Room2	1978	1781	197

Table 6. We list the number of total images (**Frames**), training sets (**Train**) and validation sets (**Validate**) for each scene.

6.2. More details of the scene representation

We use two different multi-resolution grids to store the hidden features for geometry and appearance reconstruction, including a four-level grid for geometry features and a hash-based grid for color features. Specifically, we determine the bounding box of the scene based on the GT mesh and set the voxel sizes of each level as 3cm, 6cm, 24cm and 96cm, respectively. We store 4-dim feature vectors for each resolution grid, and a 16-dim geometric feature vector is finally obtained. In addition, the setting of the hash-based grid, is identical with *InstantNGP*, including a 16 levels hash table. The coarsest level has 16 grids and the finest has 2^9. Each level interpolates a feature vector of dimension 2, obtaining a total of a 32-dimensional feature vector. The spatial hash function used is the same as *InstantNGP*:

$$h(\mathbf{x}) = \left(\bigoplus_{i=1}^{d} x_i \pi_i \right) \bmod T, \tag{19}$$

where T represents the maximum number of entries per level and the largest T is set to 2^{19}. The $\bigoplus$ denotes the bitwise exclusive OR operation, and π_i signifies distinctive, sizable prime numbers.

The coordinates of the scenes are normalized to $[-1, 1]$. The SDFs are initialized in a ball shape, which allows for filling in the empty windows smoothly and speeding up the convergence.

6.3. More details of the framework

There are four decoders in the proposed framework including the SDF decoder, density decoder, color decoder and specular decoder. Each decoder is comprised of a two-layer MLP with hidden neurons of 32. The SDF decoder and density decoder share the input with the inputting features of dimension 16 while the color decoder takes as input color feature with dimension 32. The color decoder outputs a 3-dimensional vector denoting a view-independent color and a 32-dimensional feature. The 32-dimensional feature is concatenated with the view embedding feature and subsequently fed into the specular decoder. The view embedding feature is generated via four-level Fourier position encoding for the view direction, as done in the original *NeRF*, with a dimension of 27. The specular decoder takes the concatenated feature as input and outputs view-dependent color. The learning rate for all decoders is set to 0.001 and the decay factor is set to $1/3$ at 10000 and 15000 iterations.

6.4. More details of the SDF loss functions

In order to robustly train the SDF decoder, we imposed a series of SDF losses (as shown in Eq. (20)) $\mathcal{L}_{\text{SDF}}$ to regularize

λ_d	**C-l_1 ↓**	**F-score ↑**	**PSNR ↑**	**LPIPS ↓**
0.5	0.0132	**0.985**	36.926	0.0344
2.0	0.0134	**0.985**	37.076	0.0353
5.0 (Ours)	**0.0128**	**0.985**	**37.167**	**0.0324**
10.0	0.0132	**0.985**	37.146	0.0332
50.0	0.0131	**0.985**	36.713	0.0359

Table 7. We evaluate the effect of different λ_d on the view synthesis and reconstruction. It can be seen that best performance is obtained when λ_d is 5. Worse results are achieved whenever λ_d increases or decreases.

the network as in [44]:

$$\mathcal{L}_{\text{SDF}} = \lambda_{\text{sdf}} + \lambda_{\text{fs}}\mathcal{L}_{\text{fs}} + \lambda_{\text{eik}}\,\mathcal{L}_{\text{eik}} + \lambda_{\text{smooth}}\,\mathcal{L}_{\text{smooth}}\,. \tag{20}$$

Loss $\mathcal{L}_{\text{sdf}}(x)$ is computed with Eq. (21). It calculates the distance between predicted SDF values and the real ones computed from depth value via $b(x) = D[u, v] - d$, where $D[u, v]$ is the ground truth of depth in pixel (u, v), and d is the distance between sampling points to the camera centre.

$$\mathcal{L}_{\text{sdf}}(x) = |\phi(x) - b(x)|. \tag{21}$$

Loss $\mathcal{L}_{\text{fs}}$ is used to encourage free space prediction instead of the fixed truncation values. It is computed with Eq. (22). Exponential penalty term α equal to 5 as in [44]. $\mathcal{L}_{\text{fs}}(x)$ is zero when the SDF of a query point is positive and a large value if it is negative.

$$\mathcal{L}_{\text{fs}}(x) = \max\left(0, e^{-\alpha\phi(x)} - 1, \phi(x) - b(x)\right). \tag{22}$$

The regularization term $\mathcal{L}_{\text{eik}}(x)$ encourages valid SDF predictions in unsupervised regions:

$$\mathcal{L}_{\text{eik}}(x) = (1 - \|\nabla\phi(x)\|)^2. \tag{23}$$

An explicit smoothness term is also added, named $\mathcal{L}_{\text{smooth}}(x)$, where x is randomly sampled from surface-proximal points and ϵ is a small offset in random directions set between 4mm and 1mm as in [44].

$$\mathcal{L}_{\text{smooth}}(x) = \|\nabla\phi(x) - \nabla\phi(x + \epsilon)\|^2. \tag{24}$$

Empirical results demonstrate that the above constraints increase the robustness of the training SDF process.

7. Additional Ablation Study

The effect of the depth alignment. We conduct experiments to verify the importance of λ_{align} to color decomposition. The first row and second row shown in Fig. 5 represent the experiments w/o and w/ λ_{align}, respectively. It can be seen that the depth images predicted by the model without λ_{align} are blur and the process of the color decomposition fails. With the constraint of depth alignment, the view-independent component could be extracted correctly.

Method	**C-l_1 ↓**	**F-score ↑**	**PSNR ↑**	**LPIPS ↓**
U$_\phi$ (Shared Grid)	0.0123	0.972	29.917	0.150
S$_\phi$ (Double Grids)	**0.0115**	**0.976**	**31.741**	**0.110**
U$_\sigma$ (Shared Grid)	0.0195	0.982	32.644	0.094
S$_\sigma$ (Double Grids)	**0.0168**	**0.986**	**32.744**	**0.090**

Table 8. Ablation study of the separate representation of color grids and geometric grids for indoor reconstruction. U$_\phi$ denotes the experiment that a shared four-level grid is supervised by SDF color, and S$_\phi$ represents the experiment that two separate grids are supervised by SDF color. U$_\sigma$ denotes the experiment that a shared four-level grid supervised by density color, and S$_\sigma$ represents the experiment that two separate grids supervised by density color.

The effect of λ_d. The λ_d is very important for balancing the effect of color supervision and depth supervision. Smaller λ_d results in enhancing the effect of the depth loss and reducing the effect of the view-independent color supervision. Larger λ_d increases the effect of color supervision and decreases the effect of depth supervision. We carry out experiments with the different values of λ_d ranging from 0.5 to 50. The results in Tab. 7 show that $\lambda_d = 5$ gives the best performance. In addition, the performance drops whenever λ_d is larger or smaller.

The effect of separate color and geometry representation. We design a set of experiments to validate that separate representation of color and geometry using two different feature grids gives better results than that represented by the shared one. We conducted four experiments on the "morning apartment" scene for the indoor reconstruction and view synthesis. In Tab. 8, "U" indicates the experiment with the shared grid, and "S" represents the experiment of separate grids. ϕ represents the experiment that is supervised with color generated by SDF field. σ denotes the experiment that is supervised with color generated by density field. These results show that the separate representation of the geometry field and color field provides better performance on indoor reconstruction and view synthesis under both SDF color supervision and density color supervision.

8. Additional Experimental Results

8.1. More results on two indoor datasets

Additional qualitative results in Figs. 7 and 8 of Neural-RGBD dataset and Replica dataset.

We compare the proposed method with *BundleFusion*, *Neus*, *VolSDF*, *NeuralRGBD* and *Go-Surf* in Scene *Grey-white room*, *Office2*, *Office3*, *Room0* for geometry reconstruction, as shown in Fig. 7. Our method achieves the best visual result on all indoor scenes. It can be seen from Fig. 7 that our method has richer object details and smoother planes of indoor scenes. Specifically, Our method fills in the office chair legs completely and achieves a smoother result

Methods	**Evaluation**	**office0**	**office1**	**office2**	**office3**	**office4**	**room0**	**room1**	**room2**	**Mean**
BundleFusion	C-l_1 ↓	0.0109	0.0110	0.0310	0.0660	0.0165	0.0587	0.0110	0.0339	0.0299
	F-score ↑	0.9880	0.9910	0.9190	0.8410	0.9690	0.8820	0.9900	0.9100	0.9360
	PSNR ↑	-	-	-	-	-	-	-	-	-
	LPIPS ↓	-	-	-	-	-	-	-	-	-
Neus	C-l_1 ↓	0.0154	0.2280	0.2390	0.2000	0.3440	0.2140	0.1570	0.2940	0.2288
	F-score ↑	0.2340	0.1800	0.1730	0.3050	0.0850	0.2300	0.2210	0.1240	0.1940
	PSNR ↑	33.274	33.874	26.372	26.893	28.546	25.913	28.068	28.570	28.939
	LPIPS ↓	0.1570	0.1240	0.1790	0.1640	0.1660	0.2660	0.2120	0.1790	0.1810
VolSDF	C-l_1 ↓	0.1270	0.2050	0.1820	0.2830	0.2980	0.2750	0.1580	0.2160	0.2180
	F-score ↑	0.4200	0.2440	0.4150	0.3250	0.2980	0.3280	0.3810	0.3010	0.3390
	PSNR ↑	34.327	35.733	28.996	27.943	30.595	26.374	28.807	30.227	30.375
	LPIPS ↓	0.1570	0.1120	0.1650	0.1730	0.1590	0.2660	0.2140	0.1560	0.1750
NeuralRGBD	C-l_1 ↓	0.0635	**0.0088**	0.0544	0.0177	0.3340	0.0892	0.1010	0.3480	0.1271
	F-score ↑	0.8550	0.9890	0.9380	0.9790	0.7040	0.8740	0.8420	0.5960	0.8470
	PSNR ↑	36.563	38.148	31.559	30.509	33.934	28.311	30.866	31.452	32.668
	LPIPS ↓	0.1640	0.1590	0.2000	0.1840	0.1600	0.2750	0.2410	0.2000	0.1980
GO-Surf	C-l_1 ↓	0.0099	0.0104	0.0125	0.0156	0.0133	0.0131	0.0103	0.0117	0.0121
	F-score ↑	0.9880	0.9925	0.9875	0.9825	0.9890	0.9935	0.9960	**0.9880**	0.9896
	PSNR ↑	35.105	35.655	29.059	29.138	31.784	27.378	29.522	30.096	30.967
	LPIPS ↓	0.1620	0.1740	0.2355	0.1940	0.1835	0.2975	0.2650	0.2270	0.2170
InstantNGP	C-l_1 ↓	0.2560	1.2320	0.4940	0.4940	1.1500	0.7870	0.6270	0.7900	0.7288
	F-score ↑	0.2010	0.1020	0.2660	0.2660	0.1030	0.1050	0.1510	0.0720	0.1583
	PSNR ↑	36.667	37.679	30.793	30.793	32.772	26.912	30.786	32.411	32.352
	LPIPS ↓	0.1710	0.0754	0.1240	0.1240	0.2140	0.2620	0.1350	0.0976	0.1500
DVGO	C-l_1 ↓	0.2160	0.2790	0.2010	0.3270	0.3660	0.4160	0.2470	0.3120	0.2955
	F-score ↑	0.3170	0.2040	0.3010	0.2470	0.1330	0.2360	0.2630	0.2110	0.2390
	PSNR ↑	36.859	37.878	31.596	28.349	32.583	26.985	30.250	31.192	31.962
	LPIPS ↓	0.1670	0.1640	0.2100	0.2260	0.2100	0.3500	0.2510	0.2090	0.2230
Du-NeRF	C-l_1 ↓	**0.0096**	0.0102	**0.0116**	**0.0141**	**0.0118**	**0.0119**	**0.0093**	**0.0108**	**0.0112**
	F-score ↑	**0.9890**	**0.9930**	**0.9900**	**0.9860**	**0.9910**	**0.9950**	**0.9970**	**0.9880**	**0.9911**
	PSNR ↑	**41.365**	**41.922**	**34.913**	**34.622**	**37.776**	**34.184**	**36.123**	**35.928**	**37.104**
	LPIPS ↓	**0.0546**	**0.0630**	**0.0933**	**0.0790**	**0.0775**	**0.0824**	**0.0673**	**0.0790**	**0.0740**

Table 9. Reconstruction and view synthesis results of Replica dataset. The best performances are highlighted in bold.

on the background walls and floors in the second and third columns. In the last column, our method is able to reconstruct the complete table compared to *BundleFusion*, *Neus* and *NeuralRGBD*, and refine the shape of the bottle compared to *Go-Surf*.

In addition, view synthesis performance on *Whiteroom*, *Office3*, *Room0*, and *Room1* scenes of the *Neus*, *InstantNGP*, *DVGO*, *Go-Surf* and *NeuralRGBD*, are shown in Fig. 8. Our approach achieves the best image rendering results, in both the texture-less areas and rich texture areas. For instance, we accurately restore the appearance of texture-less regions such as ceiling corners in the first column and walls in the second and third columns. Additionally, we reproduce the details of complex texture regions, such as the shutter in the third column and the stripes of the quilt in the last column. Methods that focus on view rendering such as *DVGO* and *InstantNGP* suffer in texture-less or sparsely observed regions, as shown in the first and third columns of Fig. 8. Approaches focus on surface reconstruction, such as *NeuralRGBD* and *Go-Surf*, often struggle to get good view rendering results on areas of complex texture such as the windows in the third column and the quilt in the fourth column.

The detailed quantitative results on Replica dataset and NeuralRGBD dataset can be seen in Tab. 9 and in Tabs. 11 and 12, respectively. Our method obtains the SOTA rendering performance in all scenes and gives the highest performance in most of the scenes for geometry reconstruction.

8.2. More color decomposition results

More color decomposition results are shown in Fig. 6. We can see that our method successfully decomposes the

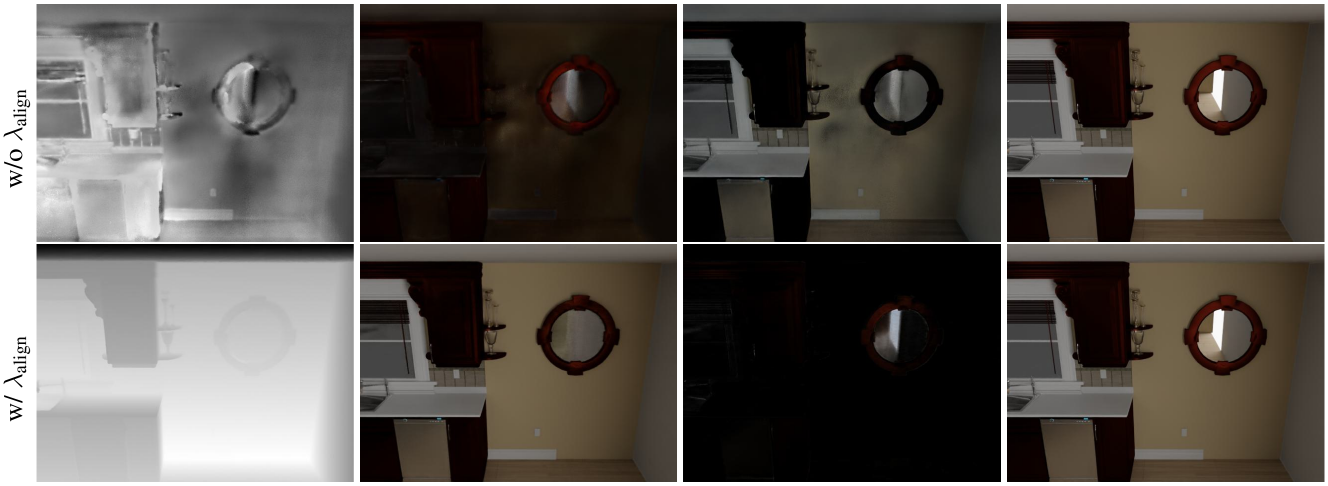

(a) Depth (b) V_i color (c) V_d color (d) GT

Figure 5. We evaluates the effect of different λ_{align} on the generated view-independent color. The first row shows the results w/o λ_{align}, while second for w/ λ_{align}. The (a), (b), (c) are the rendering depth map, view-independent color, and view-dependent color, respectively, while (d) is the complete images. The experimental results indicate that we could not get an accurate diffuse component without λ_{align}.

Scene	Scene size	Model size	Params.	Runtime
Breakfast room	$4.1 \times 3.3 \times 4.7$	116 MB	28.9 M	50 min
Green room	$8.0 \times 3.1 \times 4.7$	170 MB	42.5 M	53 min
Grey-white room	$5.9 \times 3.1 \times 4.4$	127 MB	31.7 M	50 min
ICL living room	$5.3 \times 2.9 \times 5.4$	128 MB	32.1 M	51 min
Complete kitchen	$9.3 \times 3.3 \times 10.0$	298 MB	74.1 M	73 min
Kitchen	$7.0 \times 3.4 \times 8.7$	229 MB	57.0 M	61 min
Morning apartment	$3.5 \times 2.3 \times 4.0$	81 MB	20.3 M	47 min
Staircase	$6.8 \times 3.7 \times 6.5$	206 MB	51.7 M	63 min
Thin Geometry	$3.4 \times 1.2 \times 3.6$	65 MB	16.3 M	48 min
White room	$5.6 \times 3.8 \times 7.8$	201 MB	50.3 M	59 min
Office0	$4.7 \times 5.3 \times 3.3$	130 MB	32.5 M	41 min
Office1	$5.2 \times 4.5 \times 3.3$	115 MB	28.9 M	42 min
Office2	$6.8 \times 8.5 \times 3.2$	230 MB	57.4 M	52 min
Office3	$9.0 \times 9.7 \times 3.5$	298 MB	74.5 M	70 min
Office4	$6.9 \times 6.9 \times 3.2$	193 MB	48.3 M	48 min
Room0	$8.2 \times 5.1 \times 3.2$	170 MB	42.7 M	46 min
Room1	$7.1 \times 6.1 \times 3.1$	175 MB	43.7 M	45 min
Room2	$7.2 \times 5.3 \times 4.0$	184 MB	45.9 M	46 min

Table 10. Model storage and runtime of Du-NeRF. We list *Scene size* (m^3), *Model size*, number of parameters (*Params.*) and *Runtime*. Our method reaches convergence in at most 1 hour for all scenes.

full color into view-independent color and view-dependent color such as the reflective table, the book and the TV.

9. Runtime and Memory Requirements

There is a detailed breakdown of the runtime and memory usage in our experiments on all of the datasets, as shown in Tab. 10. It can be seen that our method could reach convergence in at most 1 hour on all scenes. Similar to previous methods that trade memory for time, Du-NeRF requires hundreds of MB to store the multi-resolution grid.

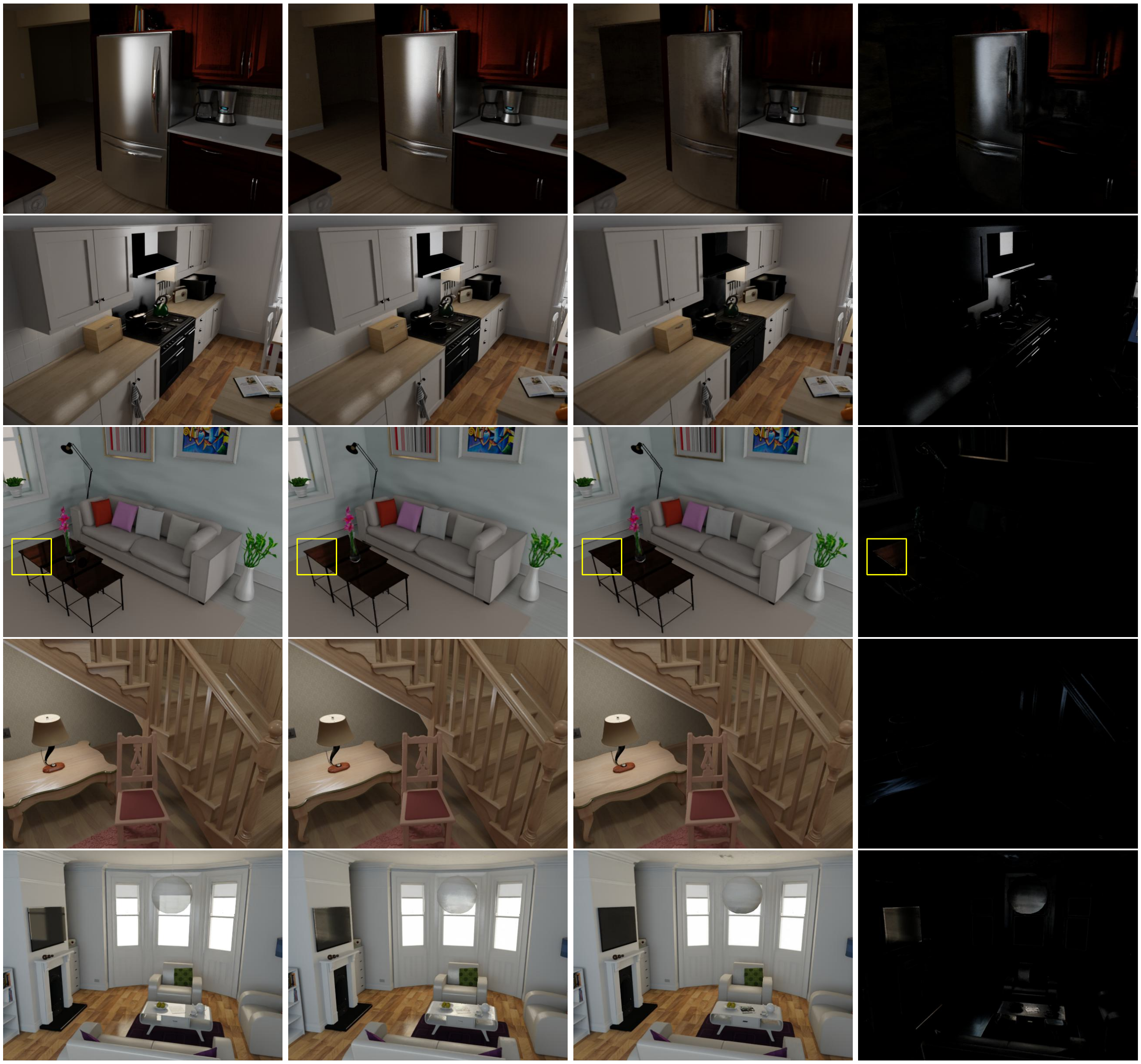

(a) GT color

(b) Rendering Color

(c) $\mathrm{V_i}$ color

(d) $\mathrm{V_d}$ color

Figure 6. More color decoupling results. The $\mathrm{V_i}$ color represents the view-independent color, while $\mathrm{V_d}$ color is the view-dependent color. It can be seen that our method can effectively decouple the complete color into the view-independent (diffusion surfaces) and view-dependent (specular reflective surfaces) colors.

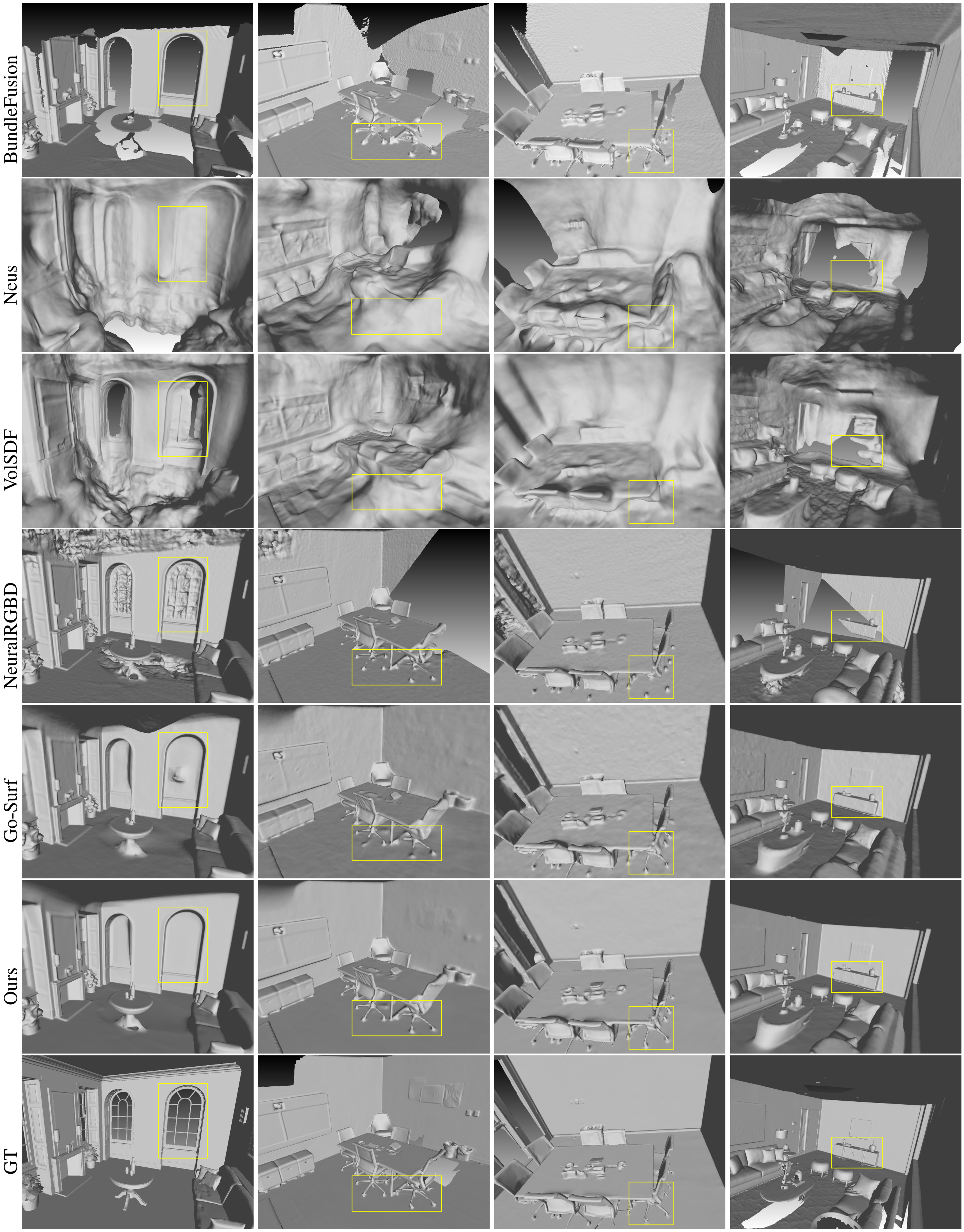

Figure 7. We show additional reconstruction results on the scene *Grey-white room*, *Office2*, *Office3* and *Room0*. Our approach allows for rich details and smoother planes highlighted in the yellow box.

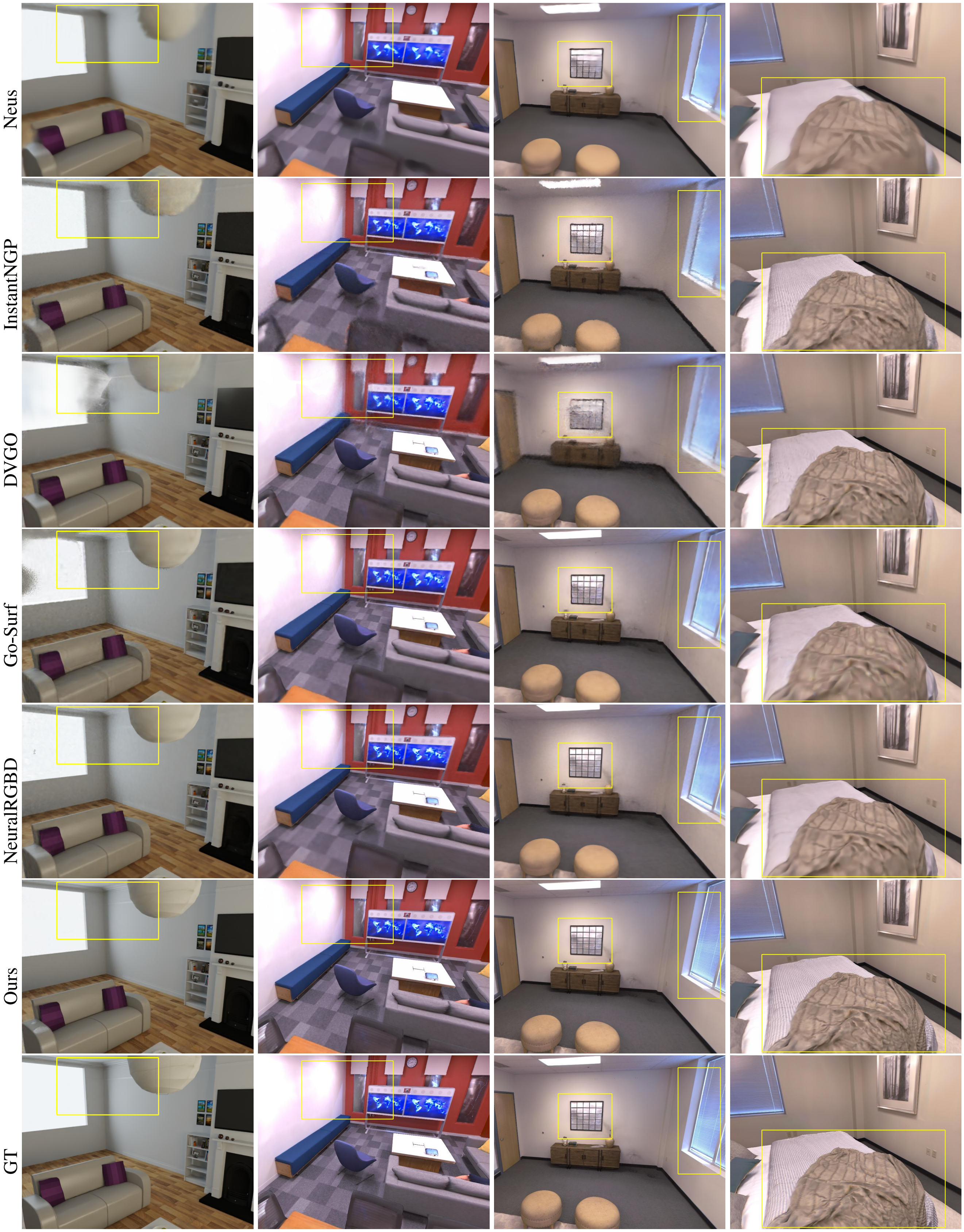

Figure 8. Additional results of view synthesis on scenes *Whiteroom*, *Office3*, *Room0*, *Room1*. The methods for novel view synthesis, such as *InstantNGP*, *DVGO*, fail to render clear results at texture-less regions, and methods focusing on geometry reconstruction, such as *Neural-RGBD*, *Go-Surf*, fail to restore the appearance of the regions with complex texture.

Scene	**Method**	**Acc** ↓	**Com** ↓	**C-l_1** ↓	**NC** ↑	**F-score** ↑	**PSNR** ↑	**SSIM** ↑	**LPIPS** ↓
Breakfast Room	BundleFusion	0.0134	0.2000	0.1070	0.9170	0.8000	-	-	-
	Neus	0.6270	0.7720	0.7000	0.6410	0.0100	27.2880	0.8230	0.1940
	VolSDF	0.0820	0.3360	0.2090	0.6880	0.2970	28.9610	0.8730	0.1570
	NeuralRGBD	0.0145	0.0148	0.0147	0.9650	0.9900	32.5340	0.9280	0.1090
	GO-Surf	**0.0141**	0.0150	0.0145	0.9630	0.9810	29.0600	0.8830	0.1650
	InstantNGP	0.2310	0.2970	0.2640	0.5670	0.2420	31.6560	0.8970	0.0853
	DVGO	0.5310	0.9010	0.7160	0.5100	0.0184	34.2720	0.9530	0.0640
	Ours	**0.0141**	**0.0135**	**0.0138**	**0.9640**	**0.9860**	**38.2610**	**0.9830**	**0.0238**
Complete Kitchen	BundleFusion	0.0366	1.0780	0.5570	0.7470	0.4450	-	-	-
	Neus	0.2950	1.5580	0.9270	0.5610	0.0641	26.3270	0.8410	0.2540
	VolSDF	0.3260	0.9100	0.6180	0.6800	0.1470	26.0160	0.8570	0.2400
	NeuralRGBD	**0.0189**	0.1100	0.0647	0.8960	0.8790	32.0310	0.9100	0.2020
	GO-Surf	0.0254	0.0295	0.0274	0.9395	0.8930	29.6040	0.8680	0.1760
	InstantNGP	0.1950	0.8730	0.5340	0.5740	0.2350	30.4066	0.8850	0.1470
	DVGO	0.2970	1.1580	0.7280	0.5610	0.1990	31.0570	0.9010	0.2180
	Ours	0.0222	**0.0259**	**0.0240**	**0.9410**	**0.9010**	**34.5170**	**0.9520**	**0.0682**
Green Room	BundleFusion	0.0140	0.1965	0.1053	0.9090	0.8140	-	-	-
	Neus	0.2130	0.3430	0.2780	0.7400	0.1130	29.4000	0.8930	0.1450
	VolSDF	0.1360	0.4320	0.2840	0.6490	0.2250	29.8840	0.9100	0.1380
	NeuralRGBD	**0.0104**	**0.0140**	**0.0122**	**0.9340**	**0.9910**	34.0800	0.9520	0.0770
	GO-Surf	0.0124	0.0156	0.0140	0.9275	0.9825	31.0520	0.9220	0.1170
	InstantNGP	0.2440	0.9710	0.6070	0.5370	0.1180	34.9470	0.9460	0.0364
	DVGO	0.2940	0.5190	0.4070	0.5640	0.2490	34.9800	0.9550	0.0760
	Ours	0.0122	0.0150	0.0136	0.9290	0.9850	**38.5530**	**0.9780**	**0.0247**
Grey White Room	BundleFusion	0.0202	0.2743	0.1472	0.8230	0.7380	-	-	-
	Neus	0.2620	0.4820	0.3720	0.6290	0.1160	28.7820	0.8630	0.1640
	VolSDF	0.1930	0.3360	0.2650	0.7070	0.2550	30.4400	0.8950	0.1480
	NeuralRGBD	**0.0134**	**0.0151**	**0.0143**	**0.9310**	**0.9940**	35.1630	0.9470	0.0900
	GO-Surf	0.0145	0.0167	0.0156	0.9255	0.9875	30.8900	0.9115	0.1490
	InstantNGP	0.1390	0.9380	0.5390	0.5010	0.1810	32.0200	0.8790	0.1270
	DVGO	0.2410	0.4430	0.3420	0.5640	0.2990	34.7160	0.9470	0.0930
	Ours	0.0140	0.0155	0.0147	0.9260	0.9900	**37.7320**	**0.9700**	**0.0406**
Icl Living Room	BundleFusion	0.0104	0.2697	0.1400	0.9120	0.7720	-	-	-
	Neus	0.3570	0.8040	0.5810	0.6270	0.1000	31.9550	0.9010	0.1090
	VolSDF	0.2520	0.8130	0.5330	0.6370	0.1450	30.6400	0.8980	0.1400
	NeuralRGBD	**0.0089**	0.0840	0.0462	0.9070	0.9010	34.3810	0.9300	0.1960
	GO-Surf	0.0101	0.0129	0.0115	0.9670	0.9910	31.7410	0.9080	0.2425
	InstantNGP	0.7180	1.8900	1.3000	0.5140	0.0100	27.1670	0.7650	0.2760
	DVGO	0.3000	0.8670	0.5830	0.5430	0.2130	33.9930	0.9330	0.2420
	Ours	0.0112	**0.0140**	**0.0126**	**0.9690**	**0.9920**	**36.9860**	**0.9570**	**0.0638**

Table 11. Reconstruction and view synthesis results of NeuralRGBD dataset. The best performances are highlighted in bold.

Scene	**Method**	**Acc** ↓	**Com** ↓	**C-l_1** ↓	**NC** ↑	**F-score** ↑	**PSNR** ↑	**SSIM** ↑	**LPIPS** ↓
Kitchen	BundleFusion	0.0170	0.5960	0.3065	0.8510	0.6390	-	-	-
	Neus	0.4680	0.8490	0.6580	0.5740	0.0400	25.5880	0.8240	0.2340
	VolSDF	0.2130	0.3760	0.2950	0.7000	0.2810	25.7570	0.8520	0.2300
	NeuralRGBD	**0.0198**	**0.1450**	0.0824	0.9000	0.8630	31.6270	0.9170	0.1480
	GO-Surf	0.0204	0.0265	**0.0235**	**0.9340**	**0.9430**	27.8260	0.8735	0.2000
	InstantNGP	0.1620	0.6470	0.4050	0.5520	0.2360	29.3850	0.8650	0.1380
	DVGO	0.2690	0.5120	0.3900	0.5640	0.3340	30.5230	0.9360	0.1310
	Ours	0.0207	0.0266	0.0236	0.9330	0.9400	**35.6100**	**0.9650**	**0.0458**
Morning Apartment	BundleFusion	0.0093	0.0153	0.0123	0.8880	0.9760	-	-	-
	Neus	0.2130	0.2430	0.2280	0.6660	0.2180	27.5640	0.8370	0.2090
	VolSDF	0.0804	0.1450	0.1130	0.7300	0.3700	29.2440	0.8870	0.1660
	NeuralRGBD	**0.0088**	**0.0117**	**0.0103**	**0.8920**	**0.9870**	33.1350	0.9270	0.1080
	GO-Surf	0.0106	0.0145	0.0125	0.8840	0.9750	28.3880	0.8570	0.2245
	InstantNGP	0.4260	0.4920	0.4590	0.5030	0.1000	24.2740	0.6230	0.4640
	DVGO	0.1510	0.1760	0.1630	0.5480	0.5100	33.9590	0.9480	0.0740
	Ours	0.0099	0.0136	0.0118	0.8870	0.9780	**36.6370**	**0.9660**	**0.0392**
Staircase	BundleFusion	0.0160	1.0020	0.5088	0.7960	0.4310	-	-	-
	Neus	0.3800	0.8910	0.6360	0.6190	0.1140	29.4540	0.8430	0.2710
	VolSDF	0.1070	0.7340	0.4200	0.6720	0.2440	30.9470	0.8490	0.2570
	NeuralRGBD	**0.0213**	0.0441	0.0327	0.9420	0.9010	34.8610	0.9070	0.2210
	GO-Surf	0.0233	0.0285	0.0259	0.9490	0.8855	32.1520	0.8805	0.2560
	InstantNGP	0.2880	0.3240	0.3060	0.5820	0.3130	31.1140	0.8250	0.2320
	DVGO	0.2710	0.7460	0.5080	0.5750	0.2580	34.5150	0.9160	0.2200
	Ours	0.0221	**0.0268**	**0.0244**	**0.9510**	**0.9280**	**36.7910**	**0.9550**	**0.0710**
Thin Geometry	BundleFusion	0.0227	0.0762	0.0495	0.8640	0.7160	-	-	-
	Neus	0.1550	0.5760	0.3650	0.5380	0.0860	19.2300	0.7830	0.1760
	VolSDF	0.1140	0.3960	0.2550	0.5990	0.2710	24.7540	0.8900	0.1360
	NeuralRGBD	0.0093	0.0254	0.0173	**0.9090**	0.9420	18.9310	0.6600	0.5580
	GO-Surf	0.0107	0.0186	0.0146	0.9005	0.9440	25.8900	0.8820	0.1400
	InstantNGP	0.0821	0.4290	0.2560	0.6130	0.3070	32.4840	0.9330	0.0347
	DVGO	0.1040	0.0750	0.0900	0.5720	0.4750	35.1540	0.9680	0.0330
	Ours	**0.0087**	**0.0122**	**0.0105**	0.9070	**0.9790**	**34.1260**	**0.9640**	**0.0286**
Whiteroom	BundleFusion	0.0184	0.8690	0.4440	0.8060	0.4700	-	-	-
	Neus	0.2040	0.3930	0.2980	0.6820	0.1710	29.0620	0.8770	0.1610
	VolSDF	0.1240	0.3370	0.2300	0.7450	0.3870	30.5300	0.9050	0.1230
	NeuralRGBD	**0.0202**	0.0437	0.0320	0.9200	0.9098	33.1980	0.9330	0.1240
	GO-Surf	0.0225	0.0359	0.0292	0.9285	0.9070	29.2535	0.8985	0.1640
	InstantNGP	0.1560	0.4570	0.3060	0.6060	0.3370	31.7830	0.9090	0.0956
	DVGO	0.2230	0.5060	0.3650	0.5880	0.3130	33.1580	0.9400	0.0970
	Ours	0.0214	**0.0340**	**0.0277**	**0.9270**	**0.9210**	**36.2280**	**0.9690**	**0.0409**

Table 12. Reconstruction and view synthesis results of NeuralRGBD dataset. The best performances are highlighted in bold.